Journal of the Meteorological Society of Japan (2026) 104:24
https://doi.org/10.1007/s44394-026-00025-4

SPECIAL EDITION: ARTICLE

Recent Advances in the Global Energy and Water Exchanges (GEWEX) Sciences

Filling observational gaps in spaceborne precipitation radars

Masafumi Hirose[1] · Shoichi Shige[2] · Takuji Kubota[3] · Shinta Seto[4] · Vasco Mantas[5] · Hatsuki Fujinami[6] · Fumie A. Furuzawa[6] · Haruya Minda[6] · Hirohiko Masunaga[6]

Received: 3 December 2025 / Accepted: 3 June 2026

Abstract

This study analyzed long-term data from the Tropical Rainfall Measuring Mission Precipitation Radar (TRMM PR) and the Dual-frequency Precipitation Radar (DPR) aboard the Global Precipitation Measurement (GPM) Core Observatory to determine inconsistencies in observation characteristics and irregular statistics related to precipitation intensity. Reference statistics were employed to quantify the effects of three observational gaps: the low-level precipitation profile (LPP) and shallow precipitation deficiency (SPD), both arising from the incidence angle dependence, and the weak precipitation deficiency (WPD), attributable to limited sensor sensitivity. The findings revealed that the LPP, the SPD, and the WPD contributed to considerable underestimation of precipitation, particularly at large incidence angles, in high-latitude areas, low-precipitation zones, and mountainous regions. Adjusting for these gaps increased overall TRMM PR precipitation estimates by approximately 12% and GPM DPR Ku-band Precipitation Radar (KuPR) precipitation estimates at higher latitudes by approximately 19%. These increases result from improved vertical representation of precipitation intensity at low altitudes and more consistent statistics for shallow and weak precipitation. Compared to the TRMM PR, the GPM DPR KuPR demonstrated stronger adjustment effects for LPP and SPD, whereas the influence of WPD was less substantial. By accounting for these effects, along with sensitivity degradation and increased clutter altitude following the orbit boosts of both satellites, the reliability of long-term, large-scale variability data is improved. Overall, this study underscores the importance of sustaining and enhancing high-precision observations of precipitation structure to resolve statistical patterns that are otherwise challenging to capture.

Keywords Spaceborne precipitation radar · Retrieval uncertainty · Observational characteristics · Shallow storm detection · Probability density function · Orbit boost effect

✉ Masafumi Hirose
mhirose@meijo-u.ac.jp

1 Faculty of Science and Technology, Meijo University, Nagoya, Japan

2 Graduate School of Science, Kyoto University, Kyoto, Japan

3 Earth Observation Research Center, Japan Aerospace Exploration Agency, Tsukuba, Japan

4 Graduate School of Engineering, Nagasaki University, Nagasaki, Japan

5 Department of Earth Sciences, University of Coimbra, Coimbra, Portugal

6 Institute for Space-Earth Environmental Research, Nagoya University, Nagoya, Japan

1 Introduction

Monitoring recent irregularities in rainfall driven by natural climate variability and anthropogenic factors has become increasingly important, making it essential to continuously evaluate and refine existing observational algorithms to improve the accuracy of current assessments and strengthen future projections (Tahroudi 2025). Microwave radiometers are primary remote-sensing instruments widely used to monitor precipitation patterns. Recent studies integrating high-precision observations have advanced drizzle-detection techniques, with some reports indicating that precipitation in certain latitudinal zones could increase by tens of percent (Jones and Kummerow 2025). However, despite these advances, current microwave radiometers still struggle to capture fine-scale precipitation features near mountainous terrain, in coastal regions, and during localized heavy-rain events (Wu and Zhao 2023). Complementing these observations, spaceborne precipitation radar offers a complementary perspective by enabling analysis of local near-surface precipitation and facilitating the evaluation of geographically enhanced observational biases (Nakamura 2021; Hirose et al. 2021). The spaceborne precipitation radar on board the Tropical Rainfall Measuring Mission (TRMM PR) operated from 1998 to 2014, while the dual-frequency precipitation radar on board the Global Precipitation Measurement (GPM DPR) core satellite has been in operation since 2014. Data from these instruments have been employed to detect near-surface precipitation echoes. Moreover, the long-term and ongoing operational periods of the both instruments have led to a continuous accumulation of data, increasing the demand for their use. In parallel, ongoing algorithmic refinements have gradually improved the reliability of retrieved precipitation estimates. Nonetheless, accurate assessment of surface precipitation remains hindered by observational gaps arising from factors such as main-lobe clutter removal and sensor sensitivity of radars, both of which can affect estimation accuracy. The clutter-free bottom (CFB) level is the altitude just above the zone affected by main-lobe clutter. This level varies depending on observation conditions and sensor parameters. Key factors include the incidence angle, underlying terrain, footprint size, and the side-lobe removal mask. This variability complicates efforts to accurately estimate low-level and surface precipitation rates. Two major observational gaps that vary with incidence angle—defined as the cross-track scan angle within approximately 17° from the nadir—are the low-level precipitation profile (LPP) and shallow precipitation deficiency (SPD). Hirose et al. (2012, 2021) proposed using near-nadir data from the lowest observable altitudes as a reference to correct the LPP and SPD in slant observations, thereby reducing incidence-angle dependence. Beyond the influence of the CFB level, weak precipitation deficiency (WPD), resulting from limited sensor sensitivity and very shallow storms, represents another major gap that can lead to underestimation.

Precipitation statistics derived from instruments with varying sensitivities, orbital observational altitudes, and CFB conditions often show low consistency. Moreover, because the effect of these gaps varies with terrain and precipitation structure, extended sampling periods are essential for robust evaluation of the latest retrieval algorithms. Spaceborne precipitation radar struggles to resolve downward variations in low-level precipitation at off-nadir viewing angles. To address this limitation, an experimental correction parameter was introduced for the LPP in the DPR Level-2 V07 product, released in 2022 (Hirose et al. 2021; Iguchi et al. 2024). More recently, Grecu et al. (2024) proposed a machine learning method that estimated the LPP using engineering-optimized profile data aligned with the 0 °C level; this method was found to be statistically valid in typical scenarios. While such approaches improve accuracy, rare localized features can still exert considerable influence and hence warrant consideration. For instance, a stratiform precipitation profile that decreases at altitudes of approximately 2–3 km and intensifies near the surface has been observed in mid- and high-latitude regions (Kobayashi et al. 2018; Hirose et al. 2021). Similarly, pronounced near-surface precipitation variations, such as coastal orographic rainfall, remain poorly characterized (Shige et al. 2017; Cheng and Yu 2019). In such cases, using data with sharp downward increases is concerning, underscoring the need for careful screening and extraction to construct representative average profiles.

Acquiring a better understanding of observational gaps in shallow storm detection using updated and long-term datasets has become increasingly essential. Precipitation structure and variability in high-elevation regions also remain poorly understood (e.g., Terao et al. 2023). Reducing clutter interference is critical for mitigating the SPD, as its influence at scan edges can extend up to 2 km, which is more than 1 km above the coverage of near-nadir observations (Shimizu et al. 2023, 2026). Observations of shallow precipitation with storm tops below 2 km remain limited because these echoes are often obscured by ground clutter at off-nadir angles, a shortfall attributed to the SPD (Hirose et al. 2021). The latest V07 algorithms for the TRMM PR and the GPM DPR enhance the detection of light precipitation through three-dimensional spatial processing (Iguchi et al. 2024), though their effectiveness in addressing the SPD has not yet been fully confirmed. In parallel, the underlying datasets have been refined through improvements such as time-varying calibration coefficients (Kanemaru et al. 2024) and adjustments for soil moisture effects (Seto et al. 2022). The use of such state-of-the-art long-term datasets, including next-generation Ku-band radar, has gained traction, with accuracy improvement based on current evaluation results remaining a pressing challenge.

At present, numerous precipitation datasets are being generated, and statistical comparisons of precipitation intensities exceeding defined thresholds are being conducted to assess retrieval errors under specific conditions (Aoki and Shige 2021; Takahashi and Fujinami 2021; Hamada and Takayabu 2016). In the near future, applying observations from high-sensitivity sensors to historical datasets may help correct the WPD—the inability to detect weak precipitation—which is a limitation highlighted in several studies using CloudSat and ground-based data (Adhikari et al. 2018; Behrangi and Song 2020; Hayden and Liu 2018; Norin et al. 2015, 2017; Schulte and Kummerow 2022). These studies interpret the absence of light precipitation as

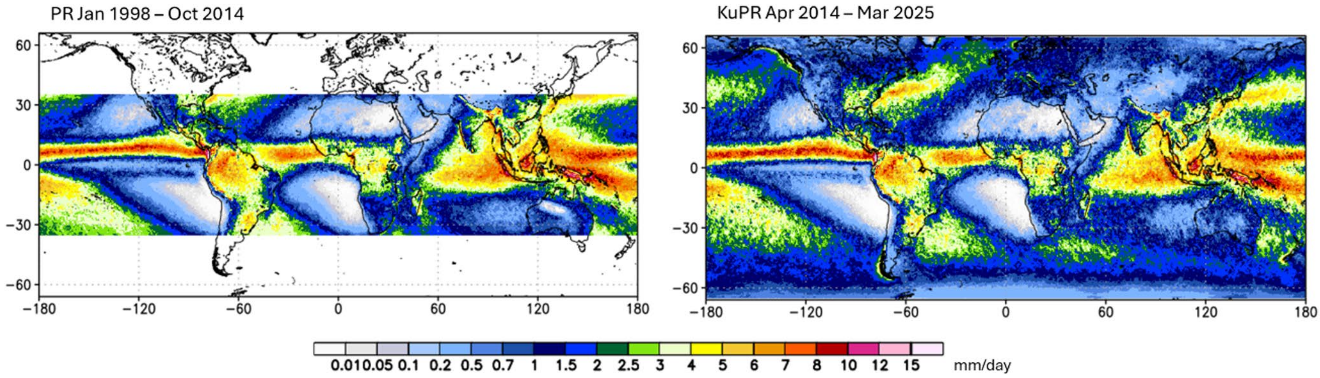

Fig. 1 Surface precipitation estimates from PR and KuPR

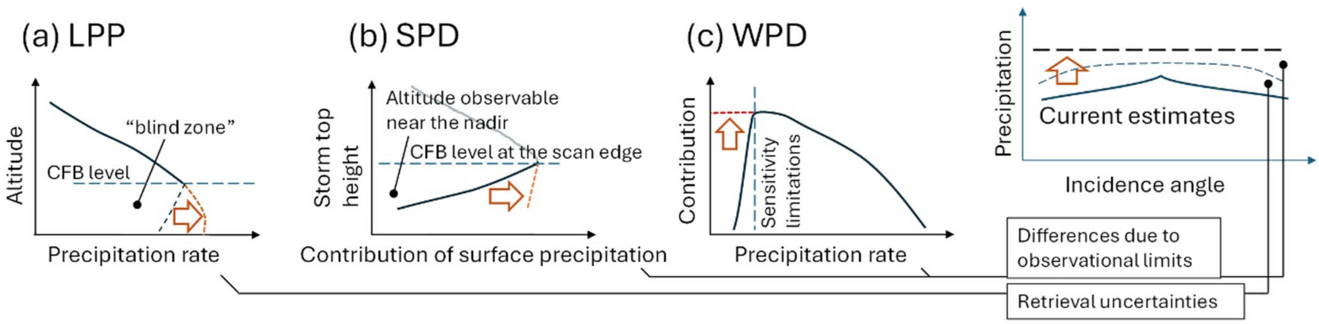

Fig. 2 Conceptual illustrations of observational gaps: **a** LPP, **b** SPD, and **c** WPD. Solid lines represent the observed statistical distributions. In (**a**), the dashed line near the surface denotes the vertical precipitation profile assumed in the standard algorithm. Orange dashed lines in (**a**–**c**) represent the ideal or reference statistics used in this study to address each gap. The rightmost panel illustrates the conceptual improvement in integrated precipitation statistics across incidence angles after applying these adjustments

a statistical discontinuity, mitigated by the more complete supplemental data provided by high-precision instruments. Nonetheless, regional and seasonal variability is expected to remain substantial. Although the GPM Ku-band precipitation radar (KuPR) offers greater sensitivity than the TRMM PR in low-latitude regions, the latter provides three times more samples overall, with an order-of-magnitude difference in sample count within the 34°–35° latitude band. Accordingly, identifying observational gaps in their corresponding datasets is essential for effective use. Integrating and comparing multiple climate datasets necessitate appropriate methods to harmonize data products originating from different sources and exhibiting varying levels of sensitivity (e.g., Seto 2022). In particular, because satellite data are acquired over long periods, database diagnostics and updates become challenging. The effects of changes in satellite altitude on operational lifespan and sensor sensitivity also require reevaluation (Hirose et al. 2012; Kubota et al. 2024; Liu et al. 2025; Shimizu et al. 2009). Because these effects are influenced by precipitation structures and their aggregate characteristics, diagnostic analyses using the latest long-term data are urgently needed. As the role of precipitation in climate change is under active investigation (Michibata 2024), ensuring the accuracy of statistical analyses, including undetected events, has become an even more critical concern.

Accordingly, in this study, the latest spaceborne precipitation radar data were analyzed to evaluate biases associated with three key observational gaps: the LPP, SPD, and WPD. To clarify the methodological framework, Sect. 2 is organized as follows: Sect. 2.1 describes the satellite datasets; Sect. 2.2 and 2.3 detail the estimation of gaps in the vertical profiles and shallow storms, respectively; and Sect. 2.4 explains the statistical approach for the undetected weak precipitation. Another objective was to assess the impacts of the incidence angle dependence and limited sensor sensitivity, including those related to the satellite orbit boost, and to address these issues to enable a more robust precipitation climatology.

2 Methods

2.1 Spaceborne precipitation radar data

TRMM PR V07 (January 1998–October 2014) and GPM DPR KuPR V07 (April 2014–March 2025) datasets (Seto 2024) were used in this analysis. The surface precipitation rate was derived from precipitation signals at the CFB level, together with assumptions applied below it (Seto et al. 2021). Although the decade-long precipitation record collected by the KuPR is based on only approximately one-third of the sample count provided by the PR in overlapping low-latitude regions, it offers detailed regional precipitation information along coastlines and mountain ranges. As demonstrated in Fig. 1, a visual comparison of the both sensors confirms that the KuPR effectively captures localized features and maintains climatological consistency with the PR despite its shorter observation period, validating its reliability for the subsequent analysis. The CFB level is the height of the lowest range bin after side-/main-lobe clutter removal. Compared to earlier versions, the CFB level was raised slightly to more effectively eliminate sidelobe clutter. Notably, the KuPR exhibits a slightly higher CFB level than the PR. In this study, "near-nadir" data refer to the central nine of the 49 scan bins. The horizontal resolutions of the footprints are approximately 5 km. To ensure statistical robustness by reducing sampling error while still capturing localized features, such as those in mountainous terrain, the analysis in this study was conducted at a 0.5° spatial resolution. Global averages were calculated by applying area weighting to the statistics. Figure 2 illustrates how the LPP, SPD, and WPD contribute to underestimation of spaceborne precipitation radar data. The arrows schematically represent statistical adjustments made to improve the consistency between different observational conditions. Although all three error types arise from observational limitations, the LPP is more appropriately classified as a retrieval uncertainty. In contrast, the SPD and WPD correspond to undetectable precipitation, and their effects are estimated statistically.

2.2 LPP

The LPP correction proposed by Hirose et al. (2021) was implemented herein; this method replaces precipitation profiles below the CFB level. An updated version of their LPP database (DB), featuring a more extensive collection of precipitation profiles and continuous data extending above the CFB level, was also adopted. This updated LPP DB v.2 is scheduled for implementation by the DPR algorithm development team to ensure consistency with the attenuation correction in the forthcoming DPR Level-2 V08 algorithm. Key updates introduced in LPP DB v.2 include the following:

1) a fivefold increase in data volume, encompassing 16 years of TRMM PR data (January 1998–December 2013) and 9 years of GPM DPR KuPR data (April 2014–March 2023);
2) application of the latest V07 product algorithm, which incorporates several improvements;
3) addition of an intensity category based on precipitation rates at 2.25–3.25 km to reduce discrepancies between observations and the a priori profile;
4) subdivision of vertical gradient categories to account for infrequent but rapid vertical changes and to eliminate discontinuities at the CFB level;
5) incorporation of nadir observations, including extremely heavy rainfall rates, into the reference statistics;
6) adjustment of CFB level settings to accumulate LPP data at altitudes 250 m higher, specifically 2.25 km for most areas and 3.25 km for mountainous regions;
7) application of comprehensive corrections for other precipitation types and storms with exceptionally high top altitudes;
8) minor revisions including temperature classification and criteria for applying average data; and.
9) implementation of vertical smoothing.

These updates enable the LPP DB v.2 to capture a broader range of precipitation patterns, including intensifying heavy rainfall and realistic gradients for light precipitation. To justify the physical validity of these vertical profile adjustments, an illustrative case study of extreme precipitation is presented here as foundational evidence for the database update. For instance, we evaluated a torrential rainfall event over the Meghalaya Plateau (orbit 071260, May 19, 2010). The surface precipitation estimates were 176, 193, and 215 mm h^{-1} when using the original data, LPP DB v.1, and LPP DB v.2, respectively. When using LPP DB v.2, a continuous downward increase was detected below the CFB level, starting near 1.5 km and reaching its maximum at 0.5 km altitude (Fig. 3). Relative to the original assumption of a constant effective radar reflectivity factor below the CFB level, LPP DB v.1 produced a + 10% correction, whereas LPP DB v.2 resulted in a + 22% correction. Similar intensification patterns were observed in other heavy rainfall cases, with precipitation intensity increasing by up to several tens of percent compared to uncorrected estimates. Notably, LPP DB v.2 comprises 44,352 profiles categorized into seven 0 °C height bins, eight precipitation intensity bins, five or six storm top height bins, three precipitation-type bins, two regional bins, 12 vertical precipitation gradient bins, and two CFB level bins. Certain profile categories contain more than 1 million samples. Despite the absence of direct observations for more than half of the database's specific conditions, profiles based on near-nadir data are generally applicable to most observation cases, enabling an adequate representation of diverse vertical profiles. Because this study is based on a simple LPP substitution, its results may differ from those of statistical evaluations conducted

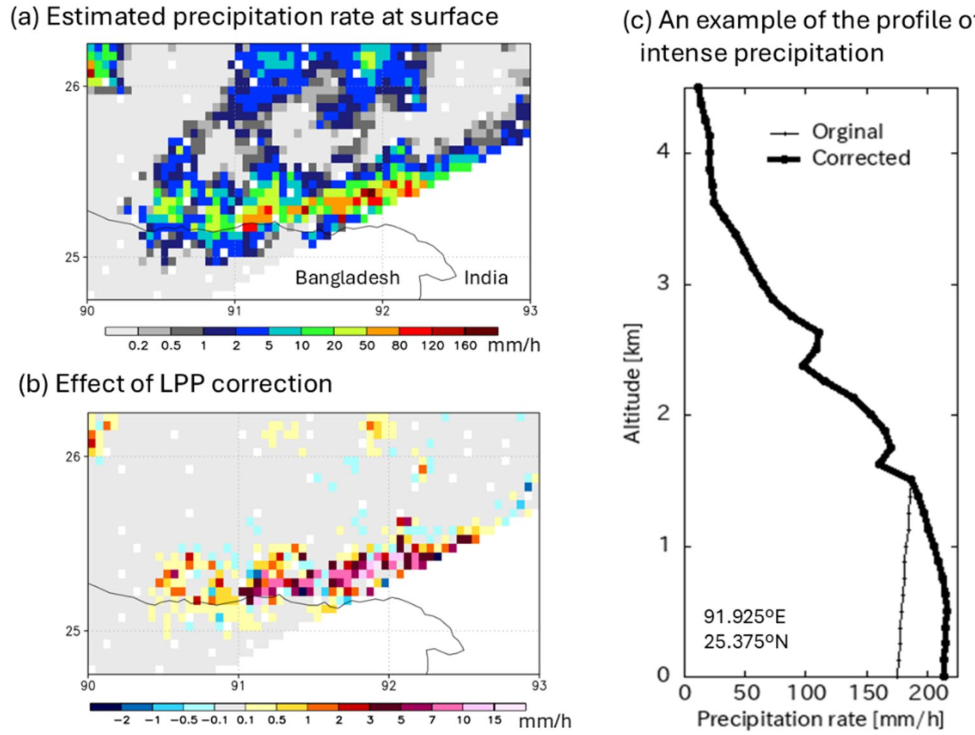

Fig. 3 Example of (**a**) precipitation estimates over the heavy rainfall area of the Meghalaya Plateau offered by TRMM PR on May 19, 2010 and **b** the difference due to the LPP correction based on LPP DB v.2. The thin and thick lines in panel (**c**) indicate the precipitation rate profiles without and with the LPP correction, respectively, at the grid cell with the maximum precipitation rate shown in (**a**)

using next-generation algorithms that enhance consistency through attenuation correction and other improvements.

2.3 SPD

Similar to the LPP, the method proposed by Hirose et al. (2021) was employed for the SPD. Specifically, missing precipitation from shallow storms was estimated by counting the number of storms (N) at each storm-top height (STH). The adjustment effect (SPD) is calculated as follows:

$$SPD = \frac{\sum_{i=1}^{49}\sum_{h=surf}^{2.5km}\sum_{k=lo/sc}\left[N\left(i,h,k\right)-N\left(nn,h,k\right)\right]\bar{R}_s\left(nn,h,k\right)}{49\sum_{h=surf}^{top}\sum_{k=lo/sc}N\left(nn,h,k\right)\bar{R}_s\left(nn,h,k\right)} \tag{1}$$

where *nn* denotes near-nadir, *lo/sc* represents categories for surface type (land/ocean) and precipitation type (stratiform/convective), and $\bar{R}_s$ is the average surface precipitation rate. Physically, the surface precipitation rate is basically positively correlated with the STH, as deeper precipitation systems generally provide more space and time for hydrometeor growth. However, this relationship varies depending on geographical and meteorological conditions; for instance, convective systems over land often show a steeper increase in intensity with STH compared to stratiform systems over the ocean. These relationships were statistically established using near-nadir data as a reference, where the CFB level is lowest and detection of shallow storms is most reliable. Statistical deviations at off-nadir angles were then translated into surface precipitation based on these established relationships at each grid. Additional methodological details regarding the SPD estimation and adjustment used in this study are provided in the supplementary materials.

Although not applied in this study, SPD is closely linked to the CFB level and shallow rain fraction, and it is also possible to estimate fine-scale effects using a lookup table (Hirose et al. 2021). A preliminary analysis revealed pronounced seasonal and regional variations in SPD. The shallow rain fraction can be derived by averaging several months of data across the extensive surrounding area. However, in regions such as the Himalayas, where precipitation characteristics vary sharply along mountain ridges, spatial smoothing introduces errors. Although other variables could enhance both temporal and spatial resolution, such refinements are beyond the scope of the present study. The current analysis focuses on long-term statistics at a 0.5° grid resolution without incorporating lookup table estimation. Our results present multi-year annual averages with minimal sampling error. However, seasonal correction results are also briefly discussed later in the text.

2.4 WPD

a. *Undetected weak precipitation*.

Our LPP and SPD analyses used near-nadir statistics as the reference. Signals missing from these observations were attributed to limited sensitivity and were thus incorporated into the WPD analysis. As the precipitation intensity decreases, the contribution of individual events diminishes; however, because the precipitation frequency increases exponentially, the integrated contribution per unit intensity remains nearly constant. This compensatory relationship suggests the frequent occurrence of numerous small-scale precipitation events with extremely weak intensities that are limited in both the horizontal extent and vertical depth. This statistical behavior is consistent with the physical framework of precipitation system near criticality (Peters and Neelin 2006), where the probability density function (PDF) follows a power-law distribution such that the contribution to the total amount remains stable at low intensities. Studies using the high-sensitivity CloudSat Cloud Profiling Radar (CPR) have confirmed that light precipitation is frequent and provides a non-negligible contribution to the total amount (Norin et al. 2015; Liang et al. 2024; Adhikari et al. 2018). Our findings also show that the PDF of the more sensitive KuPR effectively accounts for the missing weak signals in the PR data as shown later, supporting the validity of assuming a constant contribution near the sensor's limit. Regarding solid precipitation, while the contribution of weak intensity is expected to be even more significant, we adopt this constant contribution as a minimal, conservative estimate to avoid potential over-correction. Looking ahead, high-sensitivity data from EarthCARE mission, launched in 2024, will provide further insights into extremely weak precipitation. We plan to re-evaluate the probability density distributions categorized by environmental conditions as more EarthCARE data become available. Light precipitation is more prevalent in certain regions, such as off the coast of Peru. For example, the rain gauge data in the high-altitude regions of the Himalayas revealed that precipitation levels of 0.5 mm h^{-1} or less increased linearly in both frequency and total amount (see supplementary materials). Nonetheless, in this study, as schematically illustrated by the horizontal orange dashed line in Fig. 2c, the contribution per unit precipitation intensity (Cr, % mm^{-1} h) for the intensities below the minimum detectable threshold (R_{min})—where the currently observed contribution (solid line) sharply decreases—was conservatively treated as constant.

The WPD is defined as a statistical adjustment for the total precipitation climatology, derived from the PDFs of near-nadir observations to account for the aggregate contribution of undetected light precipitation. In this study, the WPD contribution was calculated as follows:

$$WPD = C_r\left(t\right) \cdot \; R_{min} - \sum\nolimits_{i=1}^{t-1} C_b\left(i\right),$$

where t denotes the minimum detectable threshold bin, and $C_b(i)$ represents the contribution of precipitation (in % bin^{-1}) at a given rainfall-rate bin i. The total precipitation observed at near-nadir angles, that is, the sum of $C_b(i)$, was defined as 100%. The *Cr(t)* is calculated as the contribution *Cb(t)* divided by the range of precipitation intensity (expressed in mm h^{-1}) of the t-th logarithmic bin, which is defined at 1 decibel of precipitation rate (dBR) intervals. Consequently, R_{min} represents the lower limit of that intensity range in absolute units. The first term in the above equation represents the contribution of precipitation intensities below R_{min}, while the second term accounts for contributions from precipitation observed below the minimum threshold. In other words, this corresponds to the portion of the curve beneath the threshold in Fig. 2c; while this threshold is fundamentally determined by sensor-specific sensitivity limitations, it is operationally treated in this study as the critical point where the observed precipitation statistics begin to shift. Unlike previous studies, which consider only precipitation above a specified threshold, this method incorporates statistics for values below the threshold. The resulting precipitation statistics ranging from 10^{-1} to $10^{2.5}$ mm h^{-1} are divided into 36 logarithmic categories. This classification corresponds to a dBR range of −10 to 25, where the precipitation rate is defined as ten times the common logarithm of the intensity. For example, the lowest category spans $10^{-1.05}$ mm h^{-1} to $10^{-0.95}$ mm h^{-1}.

In this study, the WPD estimates accounted for factors such as reduced radar sensitivity resulting from satellite altitude changes and increased surface clutter, with separate detection thresholds applied before and after the orbital adjustment. Additionally, the statistics were computed independently for each precipitation phase at the CFB height and subsequently integrated. The TRMM satellite raised its altitude by 52.5 km in August 2001, and the GPM Core Observatory similarly increased its altitude by 35 km in November 2023, thereby reducing aerodynamic drag and conserving fuel for orbit maintenance. However, radar sensitivity deteriorated, which was reflected in the observed decrease in detected precipitation (Shimizu et al. 2009; Kubota et al. 2024; Liu et al. 2025). Because the dielectric constant of ice makes solid precipitation harder to detect than liquid precipitation, this study classified precipitation into liquid and solid phases for statistical analysis. This separation is essential for accurately identifying the distinct detection of thresholds of each phase required for the WPD adjustment. The classification was based on the air temperature at the CFB level, using a threshold of 0 °C. For the TRMM PR, statistical data on the solid phase were derived from a total of 11 million near-nadir samples where the temperature at the CFB level was 0 °C or below. The occurrence frequencies of these solid and liquid precipitation samples were approximately 0.1% and 3.4%, respectively. In tropical and other warm regions where the temperature at the CFB level remains above freezing, the weighting for this solid-phase

WPD correction is effectively zero. Therefore, the correction for solid precipitation only contributes to the total amount in geographically appropriate areas, such as high-latitude regions and high-altitude mountains. The air temperature data are archived as ancillary environmental variables in the TRMM PR and GPM DPR standard products and are originally sourced from the Japan Meteorological Agency (Kubota et al. 2020a, b b; Iguchi et al. 2024). Notably, the precipitation phase cannot be determined solely by an air temperature threshold (Jennings et al. 2018, 2025; Wang et al. 2019). This study does not address the precise distinction between rain and snow at the surface. We adopt a simple temperature threshold that influences the dielectric constant near the CFB height, thereby enabling estimates of surface precipitation intensity. Assumptions regarding the particle size distributions of warm rain and snowfall may introduce systematic biases (Akiyama et al. 2025; Schulte and Kummerow 2022), necessitating continual review; however, this study evaluates these assumptions using the standard algorithm. (Fujinami et al. 2023)

b. *Statistics based on observable precipitation intensity*.

To establish the observational baselines for WPD estimation, it is necessary to analyze the statistical distribution of detectable precipitation. A probability density distribution of precipitation was constructed for each 0.5° grid cell using data obtained near the nadir. These global statistics serve as the objective foundation for determining the sensor-specific thresholds applied in our adjustment procedure. Figure 4a and b illustrate the fractions of precipitation occurrence and amount, which identify where these observational gaps emerge. As expected, the frequency of light precipitation is high, while its contribution to the total precipitation amount remains nearly constant. This stability at low intensities justifies the physical assumption of a constant contribution for the undetected weak precipitation below the sensor-specific thresholds (Figs. 4c-d). For instance, the peak contribution of the PDF identifies the baseline for setting the thresholds (t) for both sensors before and after the orbit boosts. As a numerical example of Eq. 1, if the precipitation below 0.2 mm h^{-1} is expected to contribute approximately 1% per 0.1 mm h^{-1} to the total precipitation amount, the integrated precipitation for the range below this threshold (0–0.2 mm h^{-1}) would account for approximately 2% of the observed value. Furthermore, if the current observations indicate an existing contribution of only 0.5% for this range, an additional 1.5% would be estimated as the WPD. Both the TRMM PR and the GPM DPR KuPR sensors exhibited discontinuous statistical gaps at low precipitation intensities. The deficit in PR observations is particularly pronounced. At higher latitudes, the peak of the PDF for the precipitation amount shown in Fig. 4b becomes more gradual and the intensity threshold for statistical gaps representing the discrepancy between observed and ideal statistics in Fig. 2c tends to be higher. Similarly to Fig. 4b and c shows the PDF for the precipitation amount restricted to liquid precipitation to compare the statistics before and after the orbit boost of each satellite. Figure 4d provides a corresponding representation for solid precipitation. In this context, the pre-orbit-boost period for PR (KuPR) is defined as 1998–2000 (2015–2022), while the post-orbit-boost period corresponds to 2002–2004 (2024). Data from January to December of each year was utilized here.

In this study, the lower bound of the precipitation intensity bin yielding the maximum normalized contribution *Cr* was defined as the threshold value; this corresponds to the *t*-th bin in Eq. 1, with its lower limit denoted as R_{min}.

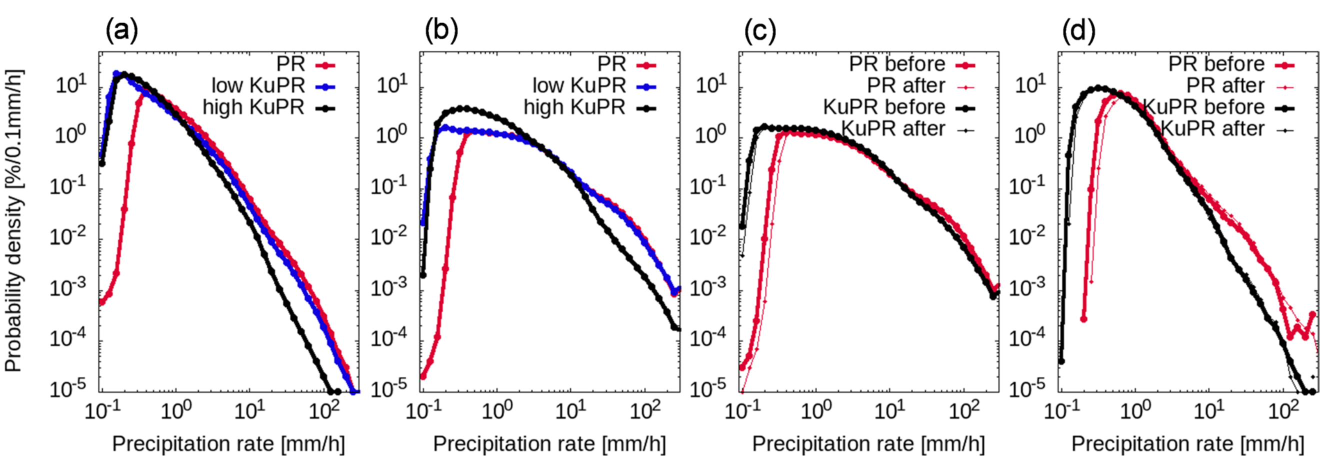

Fig. 4 PDFs of (**a**) occurrence frequency and **b**–**d** precipitation amount derived from near-nadir observations by PR and KuPR (% 0.1^{-1} mm^{-1} h). In (**a**) and (**b**), "low" and "high" KuPR data refer to those at latitudes below and above 36°, respectively. Panel (**c**) presents liquid precipitation at the CFB height before and after the orbit boost, aggregated over the full observation period and domain for each satellite. Panel (**d**) shows the corresponding results for solid precipitation

However, as discussed later, slightly higher thresholds were adopted for snowfall and for the post-orbit-boost period to mitigate the effects of missing data. Figures 4c–d illustrate that precipitation intensity declined sharply below the threshold t, which was set at the fourth bin (−7 dBR, equivalent to approximately 0.2 mm h^{-1}) for liquid precipitation and the sixth bin (−5 dBR, approximately 0.3 mm h^{-1}) for solid precipitation in the KuPR data before the orbit boost. These threshold values for KuPR-recorded precipitation are reasonable relative to those reported in previous studies (Masaki et al. 2020). Although the solid precipitation also exhibited signs of degradation owing to the limited sensitivity, the decrease in its normalized contribution Cr below the threshold was more gradual than that observed for the liquid precipitation, consistent with previous findings (Mroz et al. 2021). Following the GPM orbit boost in November 2023, the precipitation intensity associated with the peak contribution to total precipitation remained nearly unchanged; however, the detectability of weaker precipitation declined. This change is reflected in the WPD. Notably, after the orbit boost, precipitation intensities approximately 1 dB above the peak also made comparable contributions to the total. Accordingly, we set the threshold for post-orbit-boost KuPR data at a value 1 dB higher than the peak intensity. Notably, the threshold for PR differs from that of KuPR by 3 dB. The peak value shifted by 1 dB following the orbit boost due to reduced sensitivity. Accordingly, the post-boost thresholds for PR data were set to −3 dBR for liquid precipitation and −1 dBR for solid precipitation. Above these thresholds, the signal characteristics between sensors align well, and their statistical contributions remain stable and nearly constant near the threshold, despite the large variability associated with solid precipitation. Therefore, for the pre-boost period, the effect of WPD corrections for liquid precipitation in KuPR data was estimated as the difference between the product of the fourth C_r and $10^{-0.75}$ mm h^{-1} and the observed weak signal data below the threshold, as defined in Eq. 2.

The results of the WPD adjustment are reported in Sect. 3.1c; however, it should be noted that the threshold appropriately reflects the contribution of undetected weak precipitation. For example, in the WPD correction applied to TRMM PR before the orbit boost, lowering the threshold by 1 dB resulted in a 27% reduction in the correction amount compared to the correction adopted in this study, while raising it by 1 dB resulted in a 10% reduction (not shown). By setting the threshold to the precipitation intensity with the largest contribution, this estimation effectively utilizes precipitation intensity statistics near the threshold. Additionally, sensitivity experiments were conducted by changing the phase-change threshold to 1–2 °C, but no discernible impact on global statistics was observed. For example, the peak values of solid precipitation measured by KuPR after the orbit boost decreased by approximately 1%, whereas the thresholds for liquid and solid precipitation peaks remained unchanged (not shown).

Statistics based on limited samples fluctuate substantially depending on the occurrence of heavy rainfall events (Hirose et al. 2017). Therefore, the threshold was fixed with reference to these findings. Figure 5 presents a histogram of the precipitation intensity bins corresponding to the maximum normalized contribution C_r within each grid cell. This identifies the precipitation intensity range that contributes most prominently to the total precipitation at each location. This figure uses the dBR units defined in Sect. 2.4a. These dBR values correspond one-to-one with the precipitation intensities shown on the logarithmic horizontal axes of Fig. 4 (e.g., −10 dBR equals 0.1 mm h^{-1} and 0 dBR equals 1.0 mm h^{-1}), providing an alternative representation of the same intensity categories. This modal value represents a typical example of the minimum detectable precipitation intensity under conditions characterized by frequent weak precipitation. For liquid precipitation, a peak associated with the sensitivity limit appears at −7 dBR in the KuPR data, while solid precipitation exhibits a peak at −5 dBR. A secondary peak at −4 dBR is also evident for liquid precipitation, potentially reflecting the influence of other phases. Consistent with global statistics, the detectability of weak precipitation deteriorates following the orbital shift, necessitating a higher threshold for the PR data. In the PR data, the primary peaks before and after the orbit boost occur at −4 dBR and −3 dBR, respectively, displaying behavior broadly consistent with the trends shown in Fig. 4c. Following the orbital change, the threshold for the PR data was raised by 1 dB toward higher precipitation intensities, as indicated by the observational data. The mode values for the PR solid precipitation threshold and the KuPR thresholds remained unchanged following the orbit boost. However, while the results for the threshold strengthened by 1 dB were comparable to those before the boost, the results for the 1 dB weaker threshold declined markedly, with the inflection point shifting toward higher precipitation intensities. To minimize the influence of missing data on the global mean PDF, this study adopts the 1 dB stronger threshold when evaluating the impact of the orbit boost correction. These results align with the areal average described in the preceding paragraph.

Defining WPD solely based on a liquid precipitation threshold reduces its accuracy by several percent; therefore, phase separation is essential for improving WPD precision. Even at a surface temperature of 10 °C, the altitude of the CFB at the scan edge can reach approximately 2 km, where solid particles are likely detected aloft, influencing surface precipitation intensity estimates. In such cases, the low dielectric constant of ice may cause weak precipitation

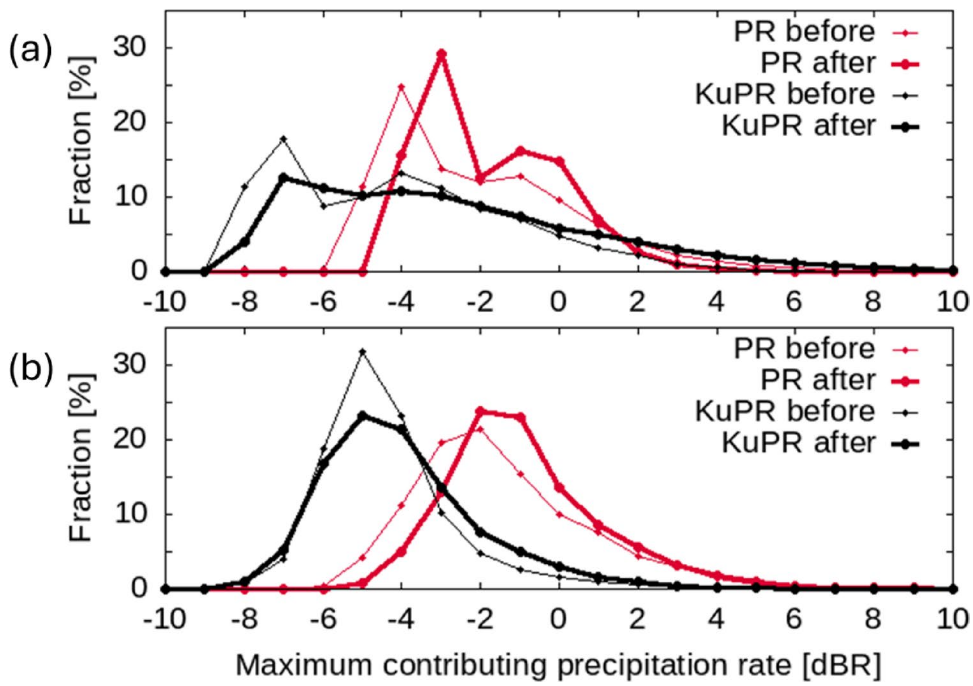

Fig. 5 Histogram of the precipitation intensity contributing most to the total at each grid cell for **a** liquid and **b** solid precipitation observed by PR and KuPR. Thin and thick lines represent the statistics before and after each satellite's orbit boost, respectively

contributions to fall below the detection threshold. Consequently, in regions and seasons where the precipitation phase changes near altitudes of 1–2 km, WPD exhibit dependence on the incidence angle (see supplementary materials). Estimating the solid-precipitation WPD at off-nadir angles using the liquid-precipitation threshold may result in a more conservative adjustment because the lower rain threshold yields a smaller *Cr* for solid precipitation, thereby preventing over-correction. However, this study estimates contributions below the detection threshold solely using statistics near the nadir, and the difference between incidence angles is addressed by LPP and SPD.

3 Results and discussion

3.1 Breakdown of precipitation underestimation

a. *LPP*.

The LPP correction in this study was derived from a globally compiled database; consequently, it increased precipitation estimates even near the nadir in mountainous regions while producing a comparable effect at off-nadir angles in mid- and high-latitude areas (Fig. 6). The former is attributable to the elevated CFB level in mountainous terrain, and the latter reflects the adjustment of shallow precipitation missed by statistically higher CFB levels occurring even near the nadir, especially in mid- and high-latitude regions where shallow profiles predominate. As the incidence angle increases, the impact of this correction becomes more prominent. In general, the correction is more effective over land and in regions with substantial rainfall, particularly for KuPR data. In some mountainous areas, the LPP correction leads to a doubling of the estimated precipitation at the scan edge. This finding underscores that when performing ground validation using limited collocated data, both the incidence angle and associated blind zone become crucial factors for interpreting the results. The blind zone refers to the region below the CFB level where surface clutter masks precipitation and LPP corrections are applied. The increase in precipitation detected by PR (KuPR) was 4% (5%) at latitudes below 36°, but for KuPR, this increase reached 32% at 60°–50° S. As illustrated in Fig. 6c, the adjustment magnitude associated with the LPP decreased at latitudes near the TRMM's inclination angle of 35°. In contrast, it rose sharply at latitudes observed only near the scan region edges. Similar to the correction using LPP DB v.1, that using LPP DB v.2 increased precipitation estimates in high-altitude regions. Light precipitation occurs frequently over the Tibetan Plateau; thus, the LPP correction exerted a particularly pronounced effect there. In the high-altitude areas and valleys of the Himalayas (86.5°–87° E, 27.5°–28° N), the correction raised precipitation estimates by 48%–67%, increasing values from 1.53 to 2.26 mm day^{-1} in the PR data and from 1.27 to 2.12 mm day^{-1} in the KuPR data. Over the Tibetan Plateau (80°–100° E, 30°–35° N), where PR data were frequently collected near the nadir, the correction contributed a 32% increase, while KuPR data, collected more extensively at the swath edges, reflected an approximate 43% increase. When the correction effect was evaluated

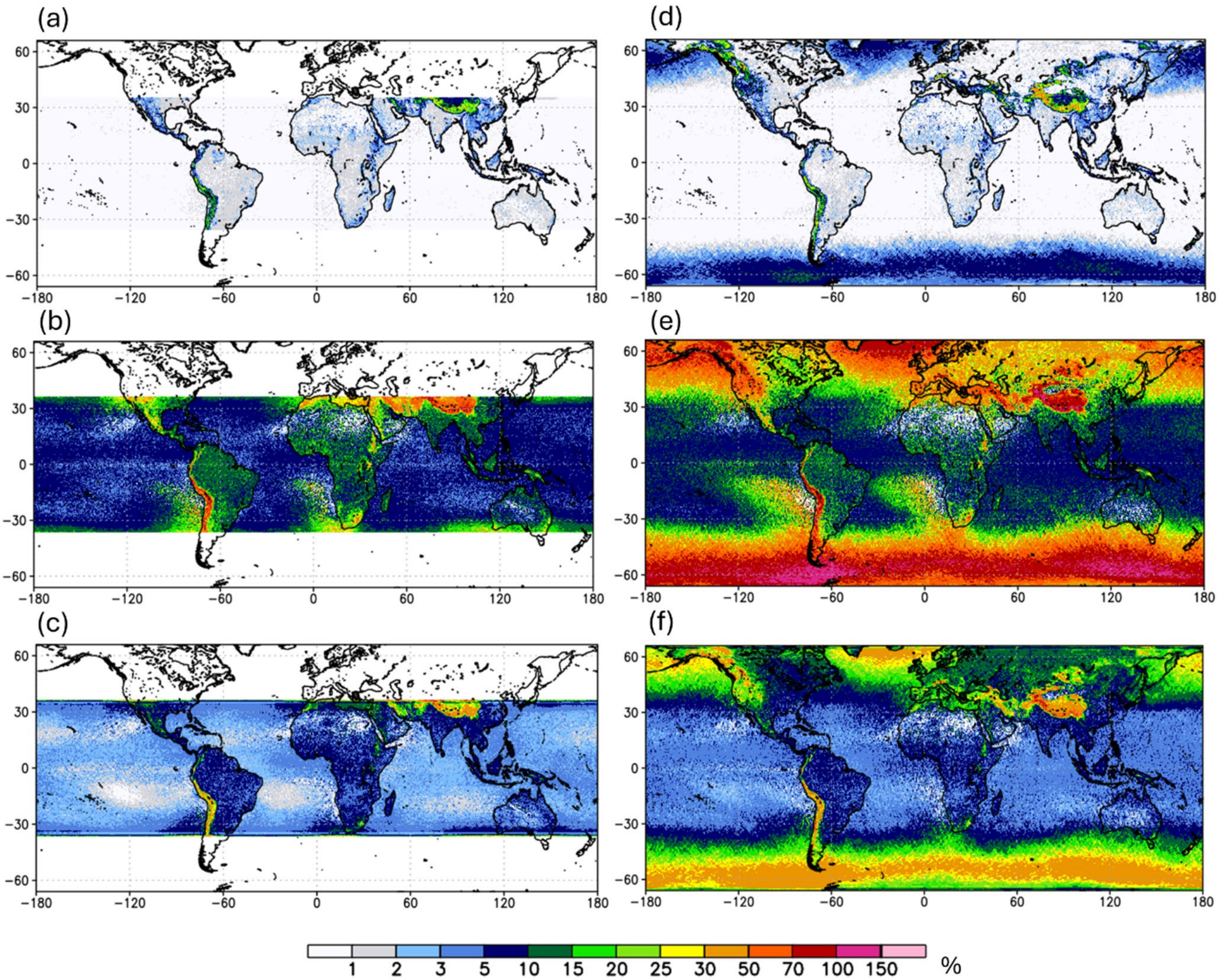

Fig. 6 Increase in estimated surface precipitation resulting from the LPP correction at near-nadir **a**, **d** swath-edge, **b**, **e** and all-angle, **c**, **f** observations from PR (**a**–**c**) and KuPR (**d**–**f**). The swath edge is defined as the outer 10 of the 49 bins

as an absolute difference, the precipitation increases were concentrated in mountainous terrain within wet regions. Notably, gains of 1 mm day^{-1} or more were recorded on the southern slopes of the Himalayas and in the vicinity of the New Guinea Highlands. As illustrated in Fig. 6f, the effect of the LPP correction diminished slightly toward the southernmost extent near 65°S, where shallow snowfall prevails (Kulie et al. 2016). This decrease suggests that in such extreme high-latitude regions, the complete omission of shallow precipitation (addressed as SPD in Sect. 3.1b) represents a more dominant error factor than the uncertainty in the vertical precipitation profile.

Figure 7 presents precipitation anomalies in the data relative to the mean from the near-nadir statistics, which serve as the reference. Regional variations in incidence angle dependence were observed, with relatively large discrepancies occurring in high-latitude regions and areas with low precipitation. At lower latitudes, underestimation was less pronounced in percentage terms but substantial in absolute magnitude. The precipitation anomaly compared to the near-nadir data was −7.1% for the TRMM PR and −8.3% for the GPM DPR KuPR equatorward of 36°, and −17.4% for the GPM DPR KuPR poleward of 36°. The LPP correction reduced these differences to −4.3% for TRMM PR and −4.5% (−5.1%) for GPM DPR KuPR at lower (higher) latitudes. At 66° S and 66° N, the median difference associated with the incidence angle dropped from −13.3% to −4.3% and from −36.8% to −24.0% at 66°–60° S, indicating that the LPP correction reduced the incidence-angle discrepancy relative to the near-nadir data by approximately half. However, PDFs before and after the correction (not shown) reveal that the statistical differences in precipitation intensities of 1 mm h^{-1} or less were not fully resolved. The remaining underestimation near 65° S and off the coast of Peru

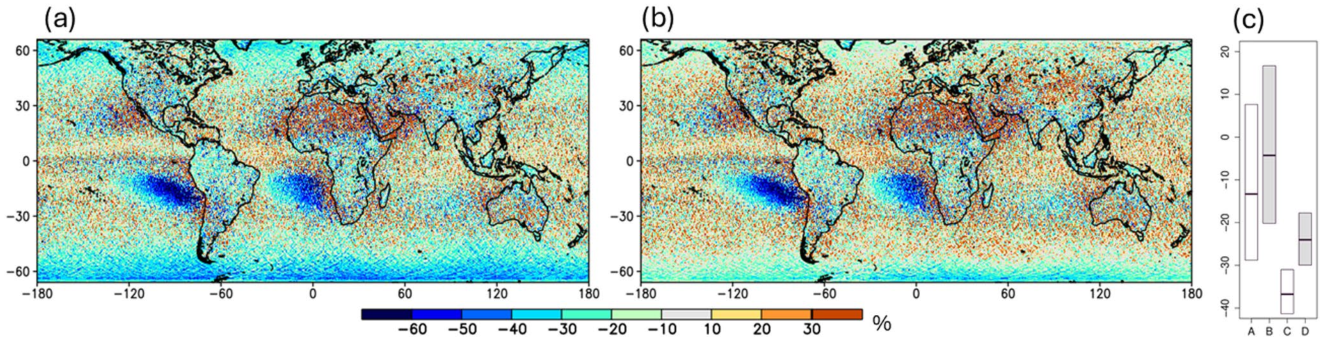

Fig. 7 Precipitation anomalies in KuPR estimates relative to the mean from the near-nadir statistics: **a** without LPP correction and **b** with LPP correction. Panel **c** presents the interquartile ranges of the anomalies for 66°S–66°N (A, B) and 66°–60°S (C, D). White (A, C) and gray (B, D) boxes denote the original and corrected data, respectively. Units are given in %

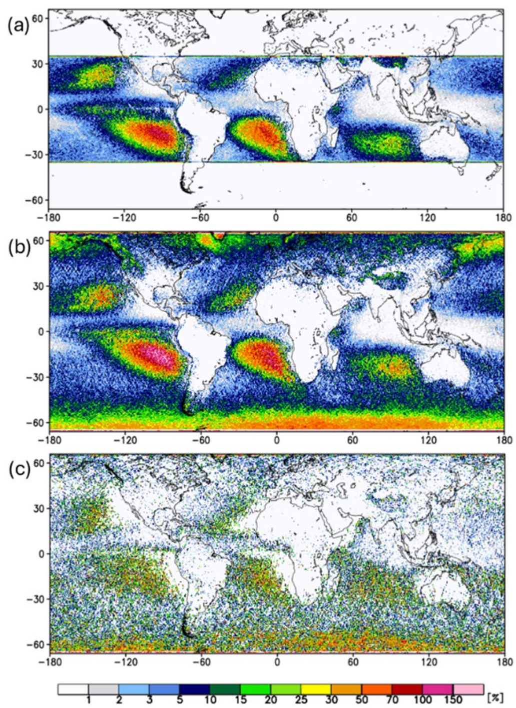

Fig. 8 Increase in estimated surface precipitation resulting from the SPD correction based on **a** 17-year PR data and **b** 11-year DPR KuPR data. The bottom panel **c** presents KuPR data from June to August 2014

is attributed to the SPD, as discussed in Sect. 3.1b. While the LPP correction introduced various profiles, including cases with increasing intensity in the downward direction, it slightly overestimated precipitation in low-precipitation regions such as deserts, suggesting a greater influence of evaporation in those areas.

Validation of extreme heavy rainfall remains a future challenge (Masunaga et al. 2019). Extremely intense precipitation events, characterized by increases exceeding 100 mm h^{-1} km^{-1} at low altitudes, were not adequately reproduced in the clutter regions. Consequently, because radars cannot resolve rapid downward increases in intensity within clutter-affected regions, the statistical representation of extreme values diverged significantly between near-nadir and off-nadir observations (not shown). Although the impact of the LPP correction and changes in total precipitation based on the presence of extreme precipitation were evident, further investigation is warranted, particularly regarding attenuation correction and spatial nonuniformity between point measurements and grid-scale averages (Tokay et al. 2014).

b. *SPD*.

As illustrated in Fig. 8, the SPD correction had a substantial impact over the ocean, where shallow storms are prevalent and often elude detection through the LPP correction, as also reported by Hirose et al. (2021). Notably, in regions such as those off the coasts of Peru and Angola, the SPD correction exceeded 100%, even at considerable distances from land. Nearly all storms in this region occur below 2.5 km altitude, making it the only area within the DPR observation domain where shallow precipitation is overwhelmingly dominant (Hirose et al. 2021). Near Antarctica, the contribution of the SPD correction became increasingly prominent in areas where the LPP correction had limited effectiveness. This statistical adjustment largely accounts for the differences shown in Fig. 7b. At the latitudinal limits of the TRMM PR coverage, only the scan-edge data are available, leading to losses exceeding 50% in regions where shallow precipitation is frequent. Compared to the results obtained by Hirose et al. (2021), who analyzed the V06 product, the estimated SPD in the present analysis increased by over 20% in oceanic regions off Peru and Angola. This increase persisted even when the definitions of near-nadir angles and the observational periods were aligned. This may reflect a greater contribution from weak precipitation resulting from improved precipitation detection methods that account for the spatial continuity of precipitation echoes (Iguchi et al. 2024). As depicted in

Fig. 8c, correction values based on three-month data exhibited marked variability even between adjacent grid points. As stated in Sect. 2.3, Hirose et al. (2021) conducted high-spatiotemporal resolution corrections by correlating the proportion of spatially averaged shallow precipitation with the clutter level. This approach enables SPD estimation even in mountainous regions where ground clutter is prominent at any given incidence angle; however, further evaluation remains necessary for indicators relevant to SPD estimation, such as the proportion of shallow precipitation identified in various mountainous areas and the precipitation profiles employed in the process. Furthermore, when sample sizes are limited, the influence of non-uniform corrections must be appropriately considered. The results presented here are interpreted as errors associated with shallow precipitation detected only near the nadir in each region. Precipitation data not captured at the near-nadir angle will be discussed in the following subsection.

c. *WPD*.

Figure 9 presents the WPD for liquid and solid precipitation based on the PR and KuPR observations using the entire available data records for the periods before and after the orbit boost, as specified at the top of each panel. As quantitatively supported by the WPD distributions in Fig. 9 and the mean values in Table 1, the KuPR demonstrates superior sensitivity relative to the PR, while the sensitivity degradation following the orbit boosts and the challenges in snow detection are also evident. These effects, which often exceed several percent, are observed broadly across the entire coverage area. Owing to limited sensitivity, missing solid

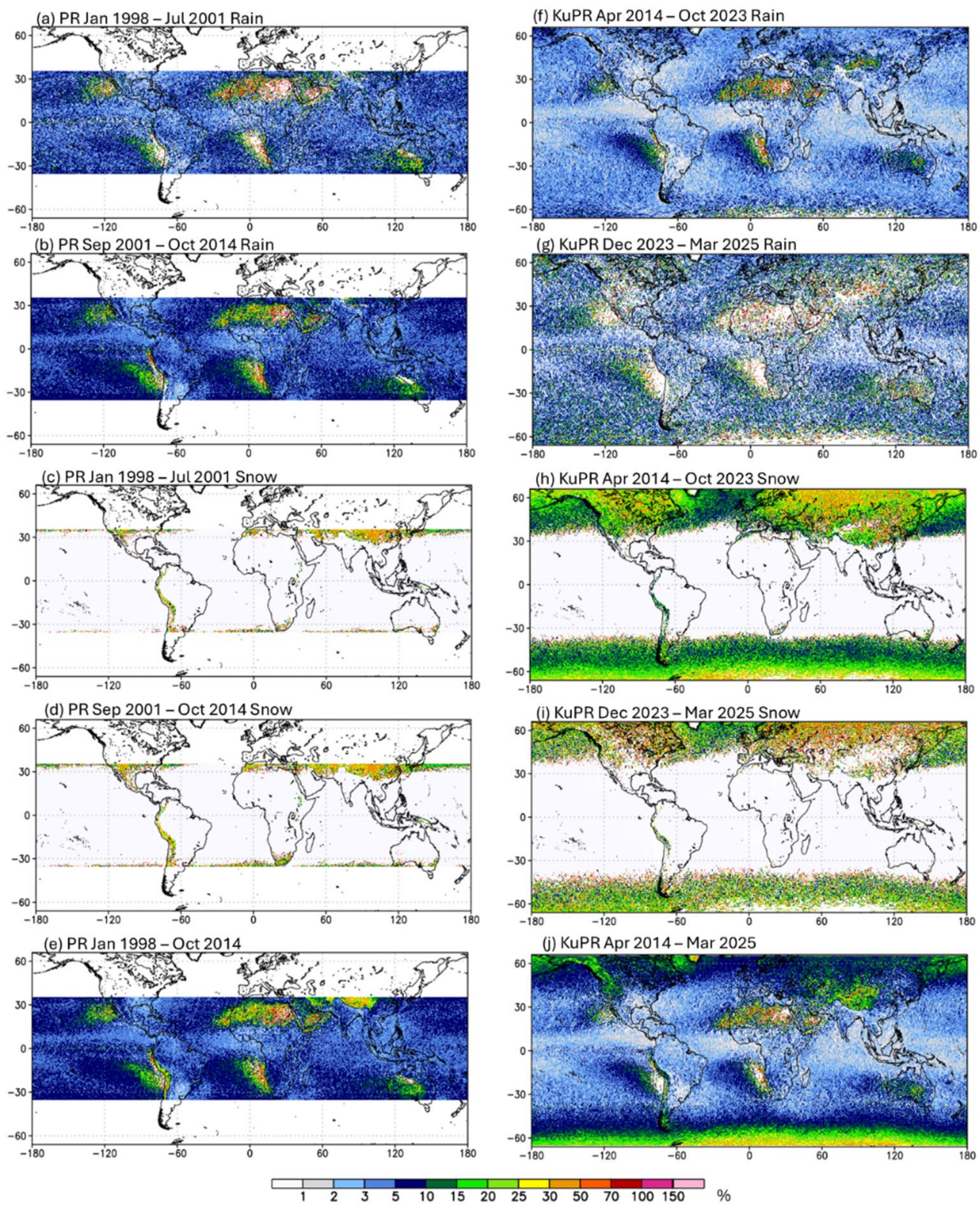

Fig. 9 Effect of WPD correction for different precipitation phases and periods at varying orbital altitudes, based on near-nadir **a**–**e** PR and **f**–**j** KuPR data. For the definitions of rain **a**, **b**, **f**, **g** and snow (**c**, **d**, **h**, **i**), as well as the periods before (**a**, **c**, **f**, **h**) and after (**b**, **d**, **g**, **i**) the orbital change, please refer to the main text. The bottom panels present the overall averages for **e** PR and **j** KuPR

precipitation estimates accounted for several tens of percent, particularly across the transoceanic storm-track region in the Southern Hemisphere (Kulie et al. 2016), which lies at a slightly higher latitude than reported in earlier studies (Hamada and Takayabu 2016). At higher latitudes, the classification of precipitation at the CFB level as solid rather than liquid influences the WPD estimation of total precipitation, reaffirming the need to apply different thresholds than those used in the tropics. Notably, for short-term datasets, missing statistics were identified in regions such as the Antarctic Ocean, Greenland, and off the coast of Peru, where precipitation amount is exceptionally low. The extent of correction in these regions became more discernible when averaged over the full observation period. To enable analyses over timeframes of several years, increasing the sample size, enhancing sensitivity, and lowering the CFB level are necessary (Shimizu et al. 2026). When the estimates below the minimum detectable threshold were excluded, namely when the second term in Eq. 1 was omitted, regions with correction values exceeding 100% became widespread in the PR solid precipitation data (not shown). This suggests that in areas with low precipitation intensity, the volume of precipitation below the threshold surpassed that above it, indicating that the estimated loss is highly sensitive to the treatment of sub-threshold data. As indicated in Table 1, which presents the WPD effect on the areal average of corrected precipitation across all regions, insufficient sensitivity in the TRMM PR led to underestimations of 4% for liquid precipitation and 27% for solid precipitation prior to the orbit boost. Based on the "All" statistics in Table 1, the WPD for the KuPR is roughly half that of the PR, and the high-latitude regions require a larger correction than the low-latitude regions. These findings confirmed that the underestimation of precipitation intensified following the sensitivity degradation caused by the orbital change, particularly for solid precipitation. For the KuPR, which modified its orbit at the end of 2023, further data collection is needed to enable more robust estimates, especially considering annual fluctuations. Nonetheless, the WPD correction values for shallow solid precipitation have slightly declined after the orbit boost, potentially due to insufficient detection of solid precipitation near the threshold.

3.2 Total gaps and their fluctuations

a. *Integrated correction.*

As discussed in the previous section, accounting for the LPP, SPD, and WPD adjustments increased the total estimated precipitation amount. The LPP and SPD results were referenced against near-nadir statistics, whereas the WPD results

Table 1 Estimated WPD, averaged over the entire region where liquid or solid precipitation occurs. "Shallow" indicates storm top heights below 2.5 km, and "Non-shallow" refers to all other cases. "BB" and "AB" represent the periods before and after the orbit boost, respectively. Units are in %

	Liquid precipitation						Solid precipitation					
	All		Shallow		Non shallow		All		Shallow		Non shallow	
	BB	AB	BB	AB	BB	AB	BB	AB	BB	AB	BB	AB
KuPR, 66° S−66° N	2.3	2.6	10.7	14.4	1.6	1.5	16.5	18.9	26.6	25.5	8.4	13.0
KuPR, 36°–66° S/N	2.8	3.6	11.4	14.8	1.7	2.0	16.6	18.9	26.5	25.4	8.4	13.0
KuPR, 36° S−36° N	2.2	2.3	10.3	14.2	1.6	1.4	14.3	17.4	30.4	31.3	9.8	13.5
PR, 36° S−36° N	3.8	4.7	13.8	18.1	3.1	3.6	26.8	27.4	40.4	35.7	20.6	23.6

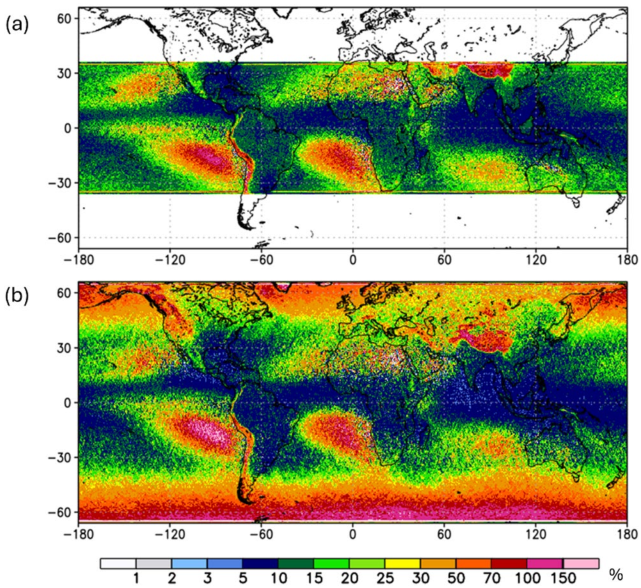

Fig. 10 Integrated correction (total bias d in Eq. 2) combining the effects of the LPP, SPD, and WPD corrections on **a** PR and **b** KuPR data

were derived solely from near-nadir data. Accordingly, all biases were calculated using the following expression:

$$d = 100 \times (1 + 0.01a + 0.01b) \times (1 + 0.01c) - 100 \quad (2)$$

where a, b, c, and d represent the effects (%) of the LPP, SPD, WPD, and total bias, respectively. The WPD components were applied separately to liquid and solid precipitation both before and after the orbit boost, and the total impact was computed by weighting each precipitation amount and the corresponding data periods. The integrated effects of LPP, SPD, and WPD adjustments are summarized in Fig. 10; Table 2. While the previous section analyzed the regional characteristics of each individual gap, the purpose of Fig. 10 is to provide a comprehensive visualization of the total observational deficiency. This integrated result accounts for the different durations of the pre- and post-orbit-boost periods for both sensors. Specifically, the statistics incorporate three years of pre-boost and thirteen years of post-boost data for the PR, and nine years of pre-boost and one year of post-boost data for the KuPR. Figure 10 serves as a critical geographical reference for the regional statistics presented in Table 3 and the overall conclusions of this study. As depicted in Fig. 10, the correction effect was shaped by the prevailing vertical precipitation structure and the CFB level, resulting in pronounced regional variability ranging from approximately 10% to tenfold that amount. Near the orbital inclination corresponding to the northern and southern edges of the TRMM observation domain, only the region around 35°, where near-nadir observations predominate, required minimal correction. Consequently, substantial corrections were needed on both

Table 2 Average precipitation after applying all three corrections. BB and AB denote the periods before and after the orbit boost, respectively. Refer to the main text for further details. The percentage values indicate the increase relative to the uncorrected estimate

	Original [mm day^{-1}]		LPP [%]		SPD [%]		WPD [%]		Total [mm day^{-1} (%)]		
	BB	AB	BB	AB	BB	AB	BB	AB	BB	AB	All
KuPR, 66° S−66° N	2.33	2.19	8.8%	9.4%	5.6%	4.8%	3.6%	5.6%	2.77 (18.6%)	2.65 (21.2%)	2.76 (18.8%)
KuPR, 36°–66° S/N	1.72	1.57	18.0%	19.3%	12.5%	10.7%	6.7%	10.0%	2.40 (40.2%)	2.26 (44.1%)	2.34 (40.5%)
KuPR, 36° S−36° N	2.68	2.54	5.1%	6.0%	3.1%	2.8%	2.4%	4.1%	2.97 (10.9%)	2.87 (13.4%)	2.96 (11.2%)
PR, 36° S−36° N	2.63	2.54	3.3%	4.2%	2.2%	3.2%	4.5%	4.9%	2.90 (10.3%)	2.86 (12.8%)	2.87 (12.3%)

Table 3 Same as Table 2, but for the selected regions. The results combining statistics before and after the orbital boost are shown. Units are mm day^{-1}

Regions	Sensors	Original	LPP	SPD	WPD	Total
India, 20°–25° N, 75°–85° E	PR	2.52	2.66 (5.8%)	2.53 (0.5%)	2.64 (4.7%)	2.80 (11.3%)
India, 20°–25° N, 75°–85° E	KuPR	2.64	2.81 (6.3%)	2.65 (0.3%)	2.72 (2.9%)	2.90 (9.8%)
Siberia, 55°–60° N, 60°–100° E	KuPR	1.12	1.25 (11.2%)	1.22 (8.1%)	1.22 (8.9%)	1.46 (30.0%)
Tibet, 30°–35° N, 80°–100° E	PR	0.38	0.50 (32.2%)	0.45 (19.9%)	0.48 (27.5%)	0.73 (93.8%)
Tibet, 30°–35° N, 80°–100° E	KuPR	0.55	0.79 (42.6%)	0.59 (5.6%)	0.64 (16.2%)	0.95 (72.3%)
Himalayas, 27.5°–28° N, 86.5°–87° E	PR	1.53	2.26 (47.8%)	1.62 (6.2%)	1.67 (9.3%)	2.57 (68.4%)
Himalayas, 27.5°–28° N, 86.5°–87° E	KuPR	1.27	2.12 (67.4%)	1.32 (4.1%)	1.38 (8.7%)	2.36 (86.4%)
Indian Ocean, 10° S−0°, 60°–95° E	PR	5.60	5.75 (2.8%)	5.68 (1.6%)	5.86 (4.7%)	6.11 (9.2%)
Indian Ocean, 10° S−0°, 60°–95° E	KuPR	5.66	5.88 (3.9%)	5.75 (1.5%)	5.78 (2.1%)	6.09 (7.5%)
Southern Ocean, 60°–55° S, 60° E−120° W	KuPR	0.95	1.28 (34.5%)	1.26 (31.9%)	1.12 (17.7%)	1.87 (96.1%)
Southern Ocean, 65°–60° S, 60° E−120° W	KuPR	0.50	0.62 (22.9%)	0.70 (40.4%)	0.63 (26.4%)	1.03 (106.2%)
Off the coast of Peru, 20°–10° S, 95°–85° W	PR	0.06	0.06 (1.9%)	0.10 (61.3%)	0.07 (11.6%)	0.11 (82.8%)
Off the coast of Peru, 20°–10° S, 95°–85° W	KuPR	0.07	0.08 (3.0%)	0.14 (97.2%)	0.08 (8.0%)	0.16 (117.0%)

sides of this latitude zone, where off-nadir observations were concentrated. At latitudes below 36°, PR and KuPR precipitation estimates increased by 12% and 11%, respectively. When the analysis was restricted to the high-latitude region observed solely by KuPR, LPP corrections and other adjustments led to a 41% increase. Furthermore, the effect extended across the entire observation area, yielding a total increase of 19%. The PR exhibited a notable response to the sensitivity adjustment (WPD), which significantly contributed to the overall precipitation increase. Consequently, the inter-sensor difference, which was 4% higher in KuPR data than in the PR data, was reduced by 1% through these adjustments, although a gap remained. The KuPR amplified the increase resulting from the LPP correction, offsetting the reduction in the WPD discrepancy achieved by the PR. The results indicate that precipitation detected by PR (KuPR) decreased by 4% (5%) following the orbital change, but this difference was reduced to 1% (3%) through correction. For KuPR in particular, the limited volume of post-boost data necessitates continued evaluation, including the influence of year-to-year variability. Discrepancies with other microwave-based observations, such as those highlighted by Hirose et al. (2021), have decreased. The gap has now narrowed to approximately 10% relative to the estimates obtained by Huffman et al. (2023) using the most recent Global Precipitation Climatology Project (GPCP) V3.2 dataset. However, as comparison precision increases, new discrepancies have begun to emerge, as discussed later.

Table 3 lists the correction results for several regions selected with consideration of the results introduced in Sect. 3.1. For land areas, the Indian subcontinent (tropical land area), inland Siberia (high-latitude land area), the Tibetan Plateau (region dominated by shallow precipitation), and the Himalayan mountain region (high-elevation area with thick ground clutter) were selected. For ocean areas, results are shown for the tropical Indian Ocean, two latitudinal bands near Antarctica, and the previously mentioned offshore Peru region. These results clearly demonstrate that the background of errors requiring correction is not uniform. They emphasize the importance of capturing the temporal and spatial aspects of factors such as geographical influences, topography, and the structure and aggregation of precipitation systems. Examples from off the coast of Peru and the Himalayan region demonstrate larger corrections when focusing on the core of low-precipitation zones. This indicates that uncertainty assessments vary significantly depending on the target being resolved.

b. *Changes in temporal variation*.

Unlike the LPP correction, which is applied to instantaneous observations, the SPD and WPD corrections are derived from statistics over a given period. Thus, care must be taken to avoid overcorrection resulting from statistically unrepresentative outliers. These corrections require sufficiently large sample sizes; even when globally averaged, estimating them using only three months of data produces a substantial discrepancy between the sum of short-term PR and KuPR corrections and the corrected values based on the full dataset. Accordingly, for the SPD and WPD, this study determined the seasonal distribution of adjustment coefficients for each sensor and period (before/after orbit changes). These coefficients were then applied to the three-month (quarterly) block averages of precipitation data to construct the long-term time series shown in Fig. 11. This quarterly averaging approach was adopted to provide a sufficient sample size for stable statistical correction while capturing seasonal variability.

Figure 11 displays the temporal variation in precipitation over the 36°S–36°N band and the mid-to-high-latitude regions (36°–66° in both hemispheres), based on three-month block averages beginning in March 1998. Following the TRMM satellite orbit change in August 2001 and the GPM Core Observatory orbit change in November 2023, estimated precipitation values decreased, while correction magnitudes increased. The adjusted data exhibit improved agreement during the overlapping observation period in the summer of 2014; however, discrepancies persist in the statistical data between the two radar sensors. During this overlapping three-month period (JJA 2014), the inter-sensor difference was reduced by 3% through correction; however, KuPR still yielded values approximately 7% higher than PR. When comparing the three years before and after the overlapping period, the difference between KuPR and PR estimates, which had previously been 5% higher for KuPR, was reduced to 1% after the integrated adjustments. The match-up analysis by Seto (2022) is generally consistent, except in cases of weak precipitation, and this discrepancy in JJA 2014 may partly stem from sampling errors over a short duration. Moreover, several observational factors are noteworthy. Specifically, the TRMM PR precipitation in JJA 2014 exhibited an unusual decrease, deviating from the typical seasonal increase observed in summer. This irregularity is likely linked to the end-of-mission status of TRMM. As reported by Hirose et al. (2023), the maximum observable altitude of the TRMM PR decreased by approximately 1 km in August 2014. Such a change in observational capability, combined with the decreasing orbital altitude, could contribute to the statistical discrepancy during this transition period. While the long-term corrected data show much better agreement, these results underscore the importance of carefully evaluating observational mode changes when comparing different sensors during mission transitions. Over the 27-year period, the estimated precipitation

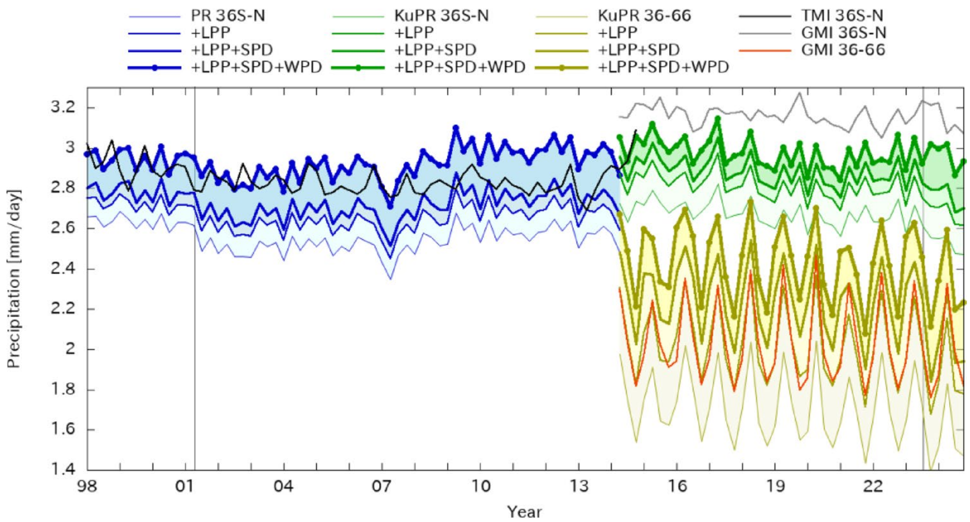

Fig. 11 Temporal variation in area-weighted average precipitation and the cumulative impact of corrections for regions below 36° latitude (36°S–36°N) and mid-to-high latitude regions (36°–66°S/N). The color-coded lines indicate precipitation levels adjusted sequentially for LPP, SPD, and WPD, as well as TMI and GMI precipitation derived from the GSMaP algorithm. The lightly shaded areas between these lines represent the incremental precipitation increase contributed by each respective correction. The data are plotted as three-month (quarterly) block averages beginning in March (MAM, JJA, SON, and DJF). The thin vertical gray lines indicate the timing of the satellite orbit changes for TRMM (August 2001) and GPM (November 2023)

trend between 36°S and 36°N shifted from an increase of 15.0 ± 7.6% to 10.5 ± 6.1% (95% confidence interval) per century after the data homogenization. Although it may be seen as an increase, the trend is not gradual.

These adjustments considerably increased the KuPR's precipitation estimates, particularly at high latitudes where shallow, large-scale precipitation systems are common and snowfall occurs during the winter. Consequently, after the adjustments, precipitation during the boreal summer approaches a magnitude more comparable to that in lower-latitude regions, effectively narrowing the previously large latitudinal gap. This substantial change underscores the need to reconsider the reference baseline used for data comparisons.

To examine the results of precipitation fluctuations after correction by comparing them with other independent data, albeit under similar sampling conditions, the time-series variation in precipitation estimates derived from observations by the TRMM Microwave Imager (TMI) and the GPM Microwave Imager (GMI), which are microwave radiometers onboard the same satellites as PR and KuPR, was also analyzed. Figure 11 presents the precipitation estimates for both the TMI and GMI computed using the GSMaP microwave radiometer algorithm V05. Both sensors yield higher precipitation estimates than the initial radar-based values; although the adjustments do not fully eliminate the discrepancy, they reduce the systematic underestimation bias. A notable feature in the comparison is that GMI estimates are approximately 10% higher than those from TMI. Furthermore, an analysis of GSMaP MVK, which integrates data from multiple satellites using infrared radiometer information, and the GSMaP Gauge, which is calibrated using the NOAA Climate Prediction Center unified rain gauge dataset (Kubota et al. 2020a, b; Mega et al. 2019), indicated that precipitation decreases by approximately 10% in both cases, while the upward tendency associated with GMI remains consistent (not shown). Furthermore, the results from the GPCP V3.2 data were also compared (see supplementary materials). Between 1998 and 2023, GPCP precipitation averaged 3.1 mm day^{-1} at latitudes below 36° and 2.8 mm day^{-1} at higher latitudes (36°–66°), showing no evidence of the aforementioned notable gap. In the low-latitude region, the GPCP precipitation more closely aligns with the GMI results, while in the high-latitude region, it displays substantially higher values than GMI. This figure again underscores the critical importance of understanding statistical gaps, including the specific characteristics of each sensor. Regarding the discrepancy observed during the transition period from TMI to GMI, the next algorithm is scheduled to incorporate improvements to the Method of Microwave Rainfall Normalization proposed by Yamamoto and Kubota (2022), and a detailed evaluation is currently being conducted by JAXA (personal communication with Dr. Yoshida). Applying insights from high-quality datasets to past observations will remain essential, with careful attention to the effects of annual variability and statistical sampling errors. Accordingly, correcting TMI statistics using the cumulative distribution function of precipitation estimated by GMI may help resolve the observed discontinuities.

For a more nuanced interpretation of the temporal variations in Fig. 11, it is worth noting that although instrumental events—such as the PR operational suspension in July 2004 and the switch to the redundant system in June 2009—could potentially influence the record, this study does not aim to evaluate these individual effects. This figure highlights that the adjustments substantially influence data interpretation and that temporal variations in the underlying phenomena must be considered when comparing statistics. Finally, although Fig. 11, based exclusively on precipitation radar or microwave radiometer data, reflects long-term fluctuations, the response to the El Niño Southern Oscillation (ENSO) and decadal oscillations (Adler et al. 2018) is less pronounced than in GSMaP_MVK or GPCP, both of which incorporate cloud information. This further underscores that algorithmic refinements, including the long-term accumulation of high-quality precipitation data and the mitigation of data gaps between instruments over land and ocean, remain major challenges with important implications.

4 Conclusion

The objective of this study was to reduce observational gaps in precipitation data derived from spaceborne precipitation radars by accounting for retrieval errors and observational limitations associated with the characteristics and temporal variations of two sensors. Major sources of precipitation underestimation, particularly differences in incidence angle, were identified and confirmed. The effect of insufficient sensitivity before and after the orbital boost was also quantitatively assessed.

Notably, improving the vertical distribution of precipitation near the surface exerts a substantial impact, enhancing precipitation intensity during heavy downpours and markedly increasing total precipitation in high-latitude regions. Across the full observational domains of the TRMM and GPM, precipitation increases by more than 10% (see Table 2). The application of the LPP to correct instantaneous profiles is anticipated to produce considerable benefits. However, even with complete elimination of LPP bias, notable underestimation would persist due to the SPD and WPD. Owing to limited sensitivity, PR underestimates liquid precipitation by 5% and solid precipitation by 27%, while KuPR detects approximately half of these cases. In this study, we compensated for the effects of the orbital changes and sensitivity differences through statistical post-processing. We confirmed that the differences before and after the orbit boost were considerably reduced; however, discrepancies remain depending on the comparison period. This indicates the need for further validation of assumptions used to estimate undetected precipitation, as well as investigations into changes in detected precipitation such as heavy rainfall and snowfall, alongside an improved understanding of annual variability.

The results concerning long-term trends suggest that, in a world where temperatures have increased by approximately 0.2 K over the past decade, precipitation data broadly align with expectations based on the Clausius–Clapeyron relationship for water vapor. However, the rate of change is considerably larger than in previous energy budget studies (Allen and Ingram 2002), interannual variability is pronounced, indicating that it does not represent a stable trend. With nearly 30 years of observations, caution remains necessary in discussing long-term precipitation trends, particularly considering observational gaps and interannual variations such as ENSO.

While the LPP can be adjusted to align with near-nadir statistics at altitudes around 1–2 km, further validation is necessary to improve the accuracy of precipitation profiles at low altitudes in mountainous regions, as well as those for extreme heavy events that intensify rapidly at lower altitudes. Trends below 1 km, difficult to observe even at nadir, may pose a considerable challenge in certain regions, particularly where terrain is steep. In such areas, profiles up to 1 km above ground level may be obscured, as noted by Terao et al. (2023). One approach to mitigate this limitation involves constraining the profile using temperature data, as implemented by Grecu et al. (2024) and in the GSMaP algorithm (Aonashi et al. 2009; Kubota et al. 2020a, b b). However, careful evaluation is required to determine the suitability of applying high-altitude profiles in tropical regions, given the contrasting near-surface conditions compared with those in mid- to high-latitude or mountainous environments. Further investigation is necessary to assess the assumptions underlying the estimation of observational limitations and to identify the features best represented through machine learning and ensemble data assimilation methods. The SPD can be estimated by associating it with the proportion of shallow precipitation (Hirose et al. 2021); however, extracting detailed spatiotemporal variability requires integration with additional variables. The WPD estimate was conservatively defined, with the contribution of liquid precipitation around 0.2 mm h^{-1} set as constant in the GPM DPR data. This paper reports the precipitation intensity threshold relevant to the WPD in decibels of precipitation rate, indicating that PR performance is degraded by 3 dB relative to that of KuPR, that solid precipitation exhibits a 2 dB degradation compared with liquid precipitation, and that post-orbit change degradation amounts to approximately 1 dB. For solid precipitation, unlike liquid precipitation, the contribution of intensity near the detection threshold to total precipitation has not been consistently captured, suggesting the influence of limited detectability.

Consequently, the WPD for solid precipitation may be underestimated. Regarding snowfall statistics, areas where contributions increase at very weak intensities have not been sufficiently detected, requiring continued efforts to identify patterns in precipitation statistics in these regions, utilizing tools such as spaceborne cloud radars and surface-based micro-rain radars (Skofronick-Jackson et al. 2019; Lemonnier et al. 2019). Owing to phase differences related to the CFB level, the correction magnitude could further increase in certain regions when accounting for sensitivity to incidence angle (see supplementary materials). Precipitation structures such as low-level bright band precipitation often undergo abrupt changes near the surface. Thus, efforts to deepen understanding of the complexity of phase discrimination continue (e.g., King et al. 2024).

In some regions, observation gaps resulted in missing precipitation data that exceeded the amount of detected data. Although refining the complex conditions in mountainous areas remains challenging, future research must continue to explore information across various spatial scales. Overall, this study underscored the importance of enhancing sensor sensitivity to mitigate the WPD effect and lowering the CFB level to minimize the LPP and SPD effects, suggesting that similar challenges may arise in other radars, such as FY-3G (Liu et al. 2025). The upcoming algorithm is expected to include improvements to the LPP and CFB level, thereby reducing uncertainty, and the ongoing accumulation and development of data call for further discussion of performance targets that exceed existing specifications. Continued efforts to supplement data within observational constraints are anticipated to promote the creation of more robust and flexible datasets. The accumulation of such complementary approaches will enhance precipitation data and Earth observation, support detection of climatic changes, strengthen water resource predictions, and advance understanding of the water cycle.

Supplementary Information The online version contains supplementary material available at https://doi.org/10.1007/s44394-026-00025-4.

Acknowledgements The authors express gratitude to members of the TRMM and GPM projects. This study was supported by the JAXA third Research Announcement on the Earth Observations (EO-RA3, PI number ER3GPF013) and fourth Research Announcement on the Earth Observations (EO-RA4, PI number ER4GPF010), and Japan Society for the Promotion of Science (JSPS) KAKENHI Grant (Number 19H01969). I would like to express my sincere gratitude to Meijo University for its generous support of my overseas research activities, which greatly contributed to the completion of this study. The authors are deeply grateful to Professor Nobuhiro Takahashi of Nagoya University for his generous guidance and many constructive comments, which greatly enhanced the authors' understanding and the overall quality of this manuscript. We are grateful to the reviewers for their constructive comments, which improved the manuscript.

Author contributions M. H. drafted the manuscript and created the figures. Sho. S., V. M., and Hi. M. critically revised the manuscript for important intellectual content, strengthening the paper's logic. T. K., Shi. S., and H. F. contributed to the provision, analysis, and interpretation of datasets within their respective areas of expertise. F. F. and Ha. M. contributed to the acquisition and analysis of the primary data and the scrutiny of the interpretation of the results. All authors reviewed the manuscript and contributed substantially to the drafting of the text.

Data availability The TRMM PR, GPM DPR KuPR, and GSMaP MVK, GSMaP Gauge data used in this study are available from the JAXA portal site. The GPCP data were downloaded from the NASA Goddard Earth Sciences Data and Information Services Center.

Declarations

Conflict of interest The authors declare no competing interests.

References

Adhikari A, Liu C, Kulie MS (2018) Global distribution of snow precipitation features and their properties from 3 years of GPM observations. J Clim 31:3731–3754. https://doi.org/10.1175/JCLI-D-17-0012.1

Adler RF, Sapiano M, Huffman GJ, Wang J, Gu G, Bolvin D, Chiu L, Schneider U, Becker A, Nelkin E, Xie P, Ferraro R, Shin DB (2018) The Global Precipitation Climatology Project (GPCP) monthly analysis (New Version 2.3) and a review of 2017 global precipitation. Atmosphere 9:4. https://doi.org/10.3390/atmos9040138

Akiyama S, Shige S, Aonashi K, Iguchi T (2025) A simple snowfall retrieval algorithm for the GPM Dual-frequency Precipitation Radar: Development and validation with OLYMPEX campaign observation. Earth Space Sci 12:e2024EA003962. https://doi.org/10.1029/2024EA003962

Allen MR, Ingram WJ (2002) Constraints on future changes in climate and the hydrologic cycle. Nature 419:224–232

Aoki S, Shige S (2021) Large precipitation gradients along the south coast of Alaska revealed by spaceborne radars. J Meteor Soc Japan 99:5–25. https://doi.org/10.2151/jmsj.2021-001

Aonashi K, Awaka J, Hirose M, Kozu T, Kubota T, Liu G, Shige S, Kida S, Seto S, Takahashi N, Takayabu YN (2009) GSMaP passive microwave precipitation retrieval algorithm: Algorithm description and validation. J Meteor Soc Japan 87A:119–136. https://doi.org/10.2151/jmsj.87A.119

Behrangi A, Song Y (2020) A new estimate for oceanic precipitation amount and distribution using complementary precipitation observations from space and comparison with GPCP. Environ Res Lett 15(124042):c

Cheng L-W, Yu C-K (2019) Investigation of orographic precipitation over an isolated, three-dimensional complex topography with a dense gauge network, radar observations, and upslope model. J Atmos Sci 76:3387–3409. https://doi.org/10.1175/JAS-D-19-0005.1

Fujinami H, Fujita K, Sato Y, Kanamori H, Kayastha R, Kayastha RB (2022) Precipitation Observations in Rolwaling Valley, eastern Nepal Himalayas, in summer 2019 [dataset]. PANGAEA. https://doi.org/10.1594/PANGAEA.943230

Fujinami H, Fujita K, Takahashi N, Sato T, Kanamori H, Sunako S, Kayastha RB (2023) Twice-daily monsoon precipitation maxima in the Himalayas driven by land surface effects. J Geophys Res Atmos 126:13. https://doi.org/10.1029/2020JD034255

Fujita K, Sunako S, Sakai A (2021) Meteorological Observations at Trakarding Glacier Automatic Weather Station, Rolwaling, Nepal, 2016–2019 [dataset]. PANGAEA. https://doi.org/10.1594/PANGAEA.931159

Grecu M, Heymsfield GM, Nicholls S, Lang S, Olson WS (2024) A machine learning approach to mitigateground clutter eff ects in the GPM combined radar-radiometer algorithm (CORRA) precipitation estimates. J Atmos Oceanic Technol 42:17-31

Hamada A, Takayabu YN (2016) Improvements in detection of light precipitation with the Global Precipitation Measurement Dual-frequency Precipitation Radar (GPM DPR). J Atmos Ocean Technol 33:653–667. https://doi.org/10.1175/JTECH-D-15-0097.1

Hayden L, Liu C (2018) A multiyear analysis of global precipitation combining CloudSat and GPM precipitation retrievals. J Hydrometeor 19:1935–1952. https://doi.org/10.1175/JHM-D-18-0053.1

Hirata H, Fujinami H, Kanamori H, Sato Y, Kato M, Kayastha RB, Shrestha ML, Fujita K (2023) Multiscale Processes Leading to Heavy Precipitation in the Eastern Nepal Himalayas. J Hydrometeor 24(4):641–658. https://doi.org/10.1175/JHM-D-22-0080.1

Hirose MS, Shimizu R, Oki T, Iguchi DA Short, Nakamura K (2012) Incidence-angle dependency of TRMMPR rain estimates. J Atmos Oceanic Technol 29:192-206

Hirose M, Takayabu YN, Hamada A, Shige S, Yamamoto MK (2017) Impact of long-term observation on the sampling characteristics of TRMM PR precipitation. J Appl Meteorol Climatol 14:713–723. https://doi.org/10.1175/JAMC-D-16-0115.1

Hirose M, Shige S, Kubota T, Furuzawa FA, Minda H, Masunaga H (2021) Refinement of surface precipitation estimates for the dual-frequency precipitation radar on the GPM core observatory using near-nadir measurements. J Meteor Soc Japan 99(5):1231–1252. https://doi.org/10.2151/jmsj.2021-060

Hirose M, Okada K, Kawaguchi K, Takahashi N (2023) Removing interfering signals in spaceborne radar data for precipitation detection at very high altitudes. J Atmos Ocean Technol 40:969–985. https://doi.org/10.1175/JTECH-D-22-0114.1

Huffman GJ, Adler RF, Behrangi A, Bovin DT, Nelkin EJ, Gu G, Ehsani MR (2023) The new version 3.2 Global Precipitation Climatology Project (GPCP) monthly and daily precipitation products. J Clim 36:21, 7635–7655. https://doi.org/10.1175/JCLI-D-23-0123.1

Iguchi T, Seto S, Meneghini R, Yoshida N, Awaka J, Le M, Chandrasekar V, Brodzik S, Tanelli S, Kanemaru K, Masaki T, Kubota T, Takahashi N (2024) GPM/DPR Level-2 Algorithm Theoretical Basis Document. 265 pp. (Available online at: https://www.eorc.jaxa.jp/GPM/doc/algorithm/ATBD_DPR_L2.pdf, accessed 1 December 2025)

Jennings KS, Winchell TS, Livneh B, Molotch NP (2018) Spatial variation of the rain-snow temperature threshold across the Northern Hemisphere. Nat Commun 9:1148

Jennings KS, Collins M, Hatchett BJ, Heggli A, Hur N, Tonino S, Nolin AW, Yu G, Zhang W, Arienzo MM (2025) Machine learning shows a limit to rain-snow partitioning accuracy when using near-surface meteorology. Nat Commun 16:2929. https://doi.org/10.1038/s41467-025-58234-2

Jones SR, Kummerow CD (2025) Improved high-latitude light precipitation estimation using a combined radiometer-cloud radar retrieval. J Geophys Res Atmos 130 e2024JD043111. https://doi.org/10.1029/2024JD043111

Kanemaru K, Iguchi T, Masaki T, Yoshida N, Kubota T (2024) Development of a precipitation climate record from spaceborne precipitation radar data. Part II: Temporal adjustment of the calibration change using the ocean normalized radar cross section. J Atmos Ocean Technol 41:921–933. https://doi.org/10.1175/JTECH-D-23-0151.1

King F, Petersen C, Fretcher CG, Geiss A (2024) Development of a full-scale connected U-Net for reflectivity inpainting in spaceborne radar blind zones. Artif lntell Earth Syst 3:e230063. https://doi.org/10.1175/AIES-D-23-0063.1

Kobayashi K, Shige S, Yamamoto MK (2018) Vertical gradient of stratiform radar reflectivity below the bright band from the Tropics to the extratropical latitudes seen by GPM. Q J R Meteorol Soc 144:21, 165–175

Kubota T, Aonashi K, Ushio T, Shige S, Takayabu YN, Kachi M, Arai Y, Tashima T, Masaki T, Kawamoto N, Mega T, Yamamoto MK, Hamada A, Yamaji M, Liu G, Oki R (2020a) Global Satellite Mapping of Precipitation (GSMaP) products in the GPM era, Satellite precipitation measurement. Springer. https://doi.org/10.1007/978-3-030-245689_20

Kubota T, Seto S, Satoh M, Nasuno T, Iguchi T, Masaki T, Kwiatkowski JM, Oki R (2020b) Cloud assumption of precipitation retrieval algorithms for the dual-frequency precipitation radar. J Atmos Ocean Technol 37:2015–2031. https://doi.org/10.1175/JTECH-D-20-0041.1

Kubota T, Masaki T, Kikuchi G, Ito M, Higashiuwatoko T, Kanemaru K (2024) Evaluation of effects on dual-frequency precipitation radar observations due to the orbit boost of the GPM core observatory. IGARSS 2024–2024 IEEE Int Geoscience Remote Sens Symp 709–712. https://doi.org/10.1109/IGARSS53475.2024.10641066

Kulie MS, Milani L, Wood NB, Tushaus SA, Bennartz R, L'Ecuyer TS (2016) A shallow cumuliform snowfall census using spaceborne radar. J Hydrometeor 17:1261–1279. https://doi.org/10.1175/JHM-D-15-0123.1

Lemonnier F, Madeleine J-B, Claud C, Genthon C, Durán-Alarcón C, Palerme C, Berne A, Souverijns N, van Lipzig N, Gorodetskaya IV, L'Ecuyer T, Wood N (2019) Evaluation of CloudSat snowfall rate profiles by a comparison with in situ micro-rain radar observations in East Antarctica. Cryosphere 13:943–954. https://doi.org/10.5194/tc-13-943-2019

Liang Y, Kou L, Huang A, Gao H, Lin Z, Xie Y, Zhang L (2024) Comparison and Synthesis of Precipitation Data from CloudSat CPR and GPM KaPR. Remote Sens 16:5. https://doi.org/10.3390/rs16050745

Liu B, Li H, Liu L, Shang J, Kuo K-S, Lu C, Yuan M, Jiang B (2025) On the detection sensitivities of dual-frequency radars onboard FY-3G and GPM-CO. Atmos Res 316. https://doi.org/10.1016/j.atmosres.2025.107935

Masunaga H, Schröder M, Furuzawa FA, Kummerow C, Rustemeier E, Schneider U (2019) Inter-product biases in global precipitation extremes. Environ Res Lett 14:12. https://doi.org/10.1088/1748-9326/ab5da9

Mega T, Ushio T, Matsuda MT, Kubota T, Kachi M, Oki R (2019) Gauge adjusted global satellite mapping of precipitation. IEEE Trans Geosci Remote Sens 57(4):1928–1935. https://doi.org/10.1109/TGRS.2018.2870199

Michibata T (2024) Radiative effects of precipitation on the global energy budget and Arctic amplification. npj Clim Atmos Sci 7:136

Mroz K, Montopoli M, Battaglia A, Panegrossi G, Kirstetter P, Baldini L (2021) Cross Validation of Active and Passive Microwave

Snowfall Products over the Continental United States. J Hydrometeor 22:1297–1315. https://doi.org/10.1175/JHM-D-20-0222.1
Nakamura K (2021) Review article progress from TRMM to GPM. J Meteor Soc Japan 99. https://doi.org/10.2151/jmsj.2021-035
Norin L, Devasthale A, L'Ecuyer TS, Wood NB, Smalley M (2015) Intercomparison of snowfall estimates derived from the CloudSat cloud profiling radar and the ground-based weather radar network over Sweden. Atmos Meas Tech 8:5009–5021. https://doi.org/10.5194/amt-8-5009-2015
Norin L, Devasthale A, L'Ecuyer TS (2017) The sensitivity of snowfall to weather states over Sweden. Atmos Meas Tech 10:3249–3263. https://doi.org/10.5194/amt-10-3249-2017
Peters O, Neelin JD (2006) Critical phenomena in atmospheric precipitation. Nat Phys 2:393–396. https://doi.org/10.1038/nphys314
Schulte RM, Kummerow CD (2022) Can DSD assumptions explain the differences in satellite estimates of warm rain? J Atmos Ocean Technol 39:1889–1901. https://doi.org/10.1175/JTECH-D-22-0036.1
Seto S (2022) Examining the consistency of precipitation rate estimates between the TRMM and GPM Ku-band radars. SOLA 18:53–57. https://doi.org/10.2151/sola.2022-009
Seto S (2024) Improvement of GPM dual-frequency precipitation radar algorithms for version 07. Adv Weather Radar 1:153–187. https://doi.org/10.1049/SBRA557F_ch5. Precipitation sensing platforms
Seto S, Iguchi T, Meneghini R, Awaka J, Kubota T, Masaki T, Takahashi N (2021) The precipitation rate retrieval algorithms for the GPM Dual-frequency Precipitation Radar. J Meteor Soc Japan 99:205–237
Seto S, Iguchi T, Meneghini R (2022) Correction of path-integrated attenuation estimates considering the soil moisture effect for the GPM dual-frequency precipitation radar. J Atmos Ocean Technol 39:6. https://doi.org/10.1175/JTECH-D-21-0111.1
Shige S, Nakano Y, Yamamoto MK (2017) Role of orography, diurnal cycle, and intraseasonal oscillation in summer monsoon rainfall over the Western Ghats and Myanmar coast. J Clim 30:9365–9381. https://doi.org/10.1175/JCLI-D-16-0858.1
Shimizu S, Oki R, Tagawa T, Iguchi T, Hirose M (2009) Evaluation of the effects of the orbit boost of the TRMM satellite on PR rain estimates. J Meteor Soc Japan 87A:83–92. https://doi.org/10.2151/jmsj.87A.83
Shimizu R, Shige S, Iguchi T, Yu C-K, Cheng L-W (2023) Narrowing the blind zone of the GPM dual-frequency precipitation radar to improve shallow precipitation detection in mountainous areas. J Appl Meteorol Climatol 62:1437–1450. https://doi.org/10.1175/JAMC-D-22-0162.1
Shimizu R, Shige S, Iguchi T, Hirose M (2026) Narrowing the blind zone of the GPM dual-frequency precipitation radar to improve shallow precipitation detection over oceans. J Meteor Soc Japan 104:6. https://doi.org/10.1007/s44394-025-00008-x
Skofronick-Jackson G, Kulie M, Milani L, Munchak SJ, Wood NB, Levizzani V (2019) Satellite estimation of falling snow: a global precipitation measurement (GPM) core observatory perspective. J Appl Meteorol Climatol 58:1429–1448. https://doi.org/10.1175/JAMC-D-18-0124.1
Tahroudi MN (2025) Comprehensive global assessment of precipitation trend and pattern variability considering their distribution dynamics. Sci Rep. https://doi.org/10.1038/s41598-025-06050-5
Takahashi H, Fujinami H (2021) Recent decadal enhancement of Meiyu-Baiu heavy rainfall over East Asia. Sci Rep 11:13665. https://doi.org/10.1038/s41598-021-93006-0
Terao T, Kanae S, Fujinami H, Das S, Dimri AP, Dutta S, Fujita K, Fukushima A, Ha K-J, Hirose M, Hong J, Kamimera H, Kayastha RB, Kiguchi M, Kikuchi K, Kim HM, Kitoh A, Kubota H, Ma W, Ma Y, Mujumdar M, Nodzu MI, Sato T, Su Z, Sugimoto S, Takahashi HG, Takaya Y, Wang S, Yang K, Yokoi S, van Oevelen P and J. Matsumoto, 2023, AsiaPEX: challenges and prospects in Asian precipitation research. *Bull. Amer. Meteor. Soc.*, E884-E908. https://doi.org/10.1175/BAMS-D-20-0220.1
Tokay A, Roche RJ, Bashor PG (2014) An experimental study of spatial variability of rainfall. J Hydrometeor 15:801–812. https://doi.org/10.1175/JHM-D-13-031.1
Wang Y-H, Broxton P, Fang Y, Behrangi A, Barlage M, Zeng X, Niu G-Y (2019) A wet-bulb temperature-based rain-snow partitioning scheme improves snowpack prediction over the drier western United States. Geophys Res Lett 46:23. https://doi.org/10.1029/2019GL085722
Wu X, Zhao N (2023) Evaluation and comparison of six high-resolution daily precipitation products in Mainland China. Remote Sens 15:223. https://doi.org/10.3390/rs15010223
Yamamoto MK, Kubota T (2022) Implementation of a rainfall normalization module for GSMaP microwave imagers and sounders. Remote Sens 14:18. https://doi.org/10.3390/rs14184445